(Received 21 January 2025, Accepted 1 April 2025, Scheduled 9 April 2025)

Robust Mode Matching of Waveguide Discontinuities by Minimizing Mean-Squared Error

James R. Nagel[1,*] and Karl F. Warnick[2]

[1] *L3Harris, Salt Lake City, Utah, USA*
[2] *Department of Electrical and Computer Engineering, Brigham Young University, Provo Utah, USA*

ABSTRACT: The Mode-Matching Method (MMM) is a numerical technique that can be used to calculate electromagnetic wave propagation through a stepped waveguide junction. We present a generalized approach to mode-matching that works by minimizing the mean-squared error (MSE) of electromagnetic boundary conditions. The process begins by expressing each component of the electromagnetic field profile as a finite summation of modes within each waveguide region. Given some arbitrary pair of mode profiles, we next calculate the squared-error of each boundary condition along the entire span of the junction. The squared error is then averaged across the junction, resulting in a single matrix-vector equation for MSE. That equation is finally differentiated with respect to the mode amplitudes, and the result is then set to zero. The solution is thus a field profile in each waveguide region that minimizes the MSE of electromagnetic boundary conditions.

1. INTRODUCTION

A fundamental building block of modern microwave engineering is the stepped waveguide discontinuity. Transformers, filters, and junctions are some of the many important radio-frequency devices that can be engineered by the appropriate cascade of discontinuities in a waveguide structure. For this reason, there exists a high demand for precise mathematical methods by which to model their behavior when excited by electromagnetic waves. In practice, this usually involves numerical simulation through such techniques as the finite-difference time-domain (FDTD) method [1] and finite-element method (FEM) [2]. While certainly reliable and accurate, such methods are also computationally intensive, and they generally lack the mathematical insight that one obtains from a more analytic approach.

Another mathematical tool that works especially well for analyzing waveguide discontinuities is called the mode-matching method (MMM) [3, 4]. Also known as the mode-matching technique (MMT), the basic idea is to compare field profiles on each side of a waveguide boundary and then calculate the mode amplitudes that best "match" the fields across it. Once these amplitudes have been found, it is relatively straightforward to calculate a complete scattering matrix between modes. The algorithm is much more efficient than traditional numerical methods, as it does not require sampling over a large number of nodes throughout the waveguide volume. Instead, it directly calculates mode amplitudes from the geometry itself, and computational complexity is constrained only by the total number of desired modes in the solution.

Despite having been introduced many decades ago, the mathematical foundations of MMM are not nearly as well-developed as those for FEM or FDTD. In particular, the method does not yet generalize well over a broad set of possible waveguide boundaries. The reason appears to be rooted in the original solution method itself [4], which is based on a naive exploitation of mode orthogonality. While this provides satisfying results for simple open/constricted waveguide boundaries, it does not accurately model more complex geometries like offset waveguides, irises, or mismatched dielectric loads. This severely limits the practical value of MMM, and it likely explains the limited use throughout industry.

In this paper, the authors build upon the original MMM concept to develop a rigorous numerical technique that generalizes over a much broader range of possible waveguide boundaries. Rather than relying on mode orthogonality, we instead calculate the mean-squared error (MSE) across the electromagnetic boundary conditions. For many practical waveguide geometries, this error can be exactly quantified and minimized, thus yielding a mathematically optimal solution for any finite number of mode amplitudes. The basic principle was originally developed for Laplace equations with mixed boundary conditions [5], and it was further built upon to generate a finite-series solution to the classic microstrip/stripline transmission line [6]. In this work, we apply the same principle to the case of a parallel-plate waveguide with a stepped discontinuity. We then conclude with a brief discussion of further potential applications.

2. BACKGROUND

Figure 1 depicts the full system geometry for two parallel-plate waveguides joined together at $x = 0$. On the left is Region 1 ($x < 0$), which has a plate separation of h_1 and a y-offset of y_1. Between the plates, the material properties are given by the

* Corresponding author: James R. Nagel (nageljr@gmail.com).

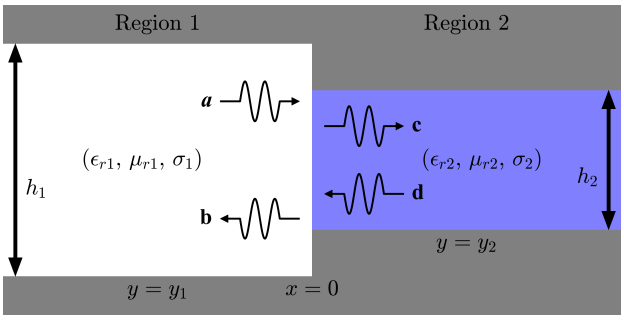

FIGURE 1. Model parameters for a stepped discontinuity between two parallel plate waveguides.

dielectric constant ϵ_{r1}, relative permeability μ_{r1}, and electrical conductivity σ_1. On the right is Region 2 ($x > 0$) which has the corresponding parameters h_2, y_2, ϵ_{r2}, μ_{r2}, and σ_2.

The basic theory of electromagnetic wave propagation through a parallel-plate waveguide is well-documented in many standard textbooks [7–9]. However, when two waveguides are joined together at a discontinuous junction, the standard mathematical notation tends to struggle at tracking the numerous parameters. We therefore begin with the classical theory of waveguide modes, but adjust the usual notation in order to simplify development of the proposed solution method.

The principle insight from waveguide theory is that any arbitrary field profile may be expressed as a linear combination of discrete modes propagating in the forward ($+\hat{\mathbf{x}}$) and reverse ($-\hat{\mathbf{x}}$) directions. In this scenario, we imagine an incident field profile in Region 1 that propagates to the the right and excites the junction. The incident field profile is completely described by the mode vector $\boldsymbol{a}$, which is a column vector of complex mode amplitudes given by

$$\boldsymbol{a} = [a_1,\, a_2,\, a_3,\, \ldots]^T. \tag{1}$$

For many practical scenarios, it is common to excite the junction with just the fundamental mode. This usually implies unit value for a_1, followed by zeros for all subsequent a_n. In general, however, the excitation profile may consist of any arbitrary combination of nonzero modes. For example, a cascade of many junctions would excite higher-order modes due to scattering, as well as reflected modes that excite the junction in the opposite direction. Thus, for generality, we may further assume an incident field profile propagating to the left from Region 2, and we describe that profile by the mode vector $\mathbf{d}$.

Upon striking the waveguide junction, two more fields reflect away, and these are described by the mode vectors $\mathbf{b}$ and $\mathbf{c}$. In principle, the mode vectors $\boldsymbol{a}$, $\mathbf{b}$, $\mathbf{c}$, and $\mathbf{d}$ may be infinite in length, and any real-world field profile would necessarily require an infinite number of modes to perfectly express it. In practice, however, computers have only finite memory, which means that the actual length of each vector must be truncated to some positive integer N.

Two polarization states are possible for the junction. The first case is known as transverse magnetic (TM) polarization, which is defined by an auxiliary magnetic field with no z-component (i.e., $\mathbf{H} \cdot \hat{\mathbf{z}} = 0$). For a parallel-plate waveguide, this implies an electric field $\mathbf{E}$ that points entirely along the $\hat{\mathbf{z}}$ direction (i.e., $\mathbf{E} = \hat{\mathbf{z}}E_z$), and we refer to this as the *primary* field component. The auxiliary magnetic field $\mathbf{H}$ will then have components along both the $\hat{\mathbf{x}}$ and $\hat{\mathbf{y}}$ directions, and we refer to them as the *secondary* field components. Likewise, a transverse electric (TE) wave is defined by the opposite, with $\mathbf{H} = \hat{\mathbf{z}}H_z$ serving as the primary field and (E_x, E_y) serving as the secondary components.

Beginning with TM polarization, we imagine an electromagnetic wave propagating to the right and exciting the junction from Region 1. The primary field component is thus the electric field, and we may express the incident, or forward-propagating, wave as

$$\mathbf{E}_1^+(x,y) = \hat{\mathbf{z}} \sum_{n=1}^{\infty} a_n \psi_n^{(1)} e^{-j\gamma_n^{(1)} x} \qquad (x \le 0). \tag{2}$$

The nth basis function $\psi_n^{(1)}$ for Region 1 is then defined as

$$\psi_n^{(1)}(y) = \begin{cases} \sin\left(\kappa_n^{(1)}(y - y_1)\right) & y \in [y_1, H_1] \\ 0 & \text{otherwise} \end{cases} \tag{3}$$

where $H_1 = y_1 + h_1$ is the ceiling height in Region 1. The nth transverse propagation constant is then given by $\kappa_n^{(1)} = n\pi/h_1$.

Due to the presence of physical material between the waveguide plates, the intrinsic wavenumber k_1 of the medium is given as

$$k_1 = \omega\sqrt{\mu_1 \epsilon_{c1}}, \tag{4}$$

where $\omega = 2\pi f$ is the angular frequency of excitation. The complex permittivity is then calculated using

$$\epsilon_{c1} = \epsilon_0 \epsilon_{r1} - j\,\frac{\sigma_1}{\omega}. \tag{5}$$

Using the dispersion relation, we then calculate the longitudinal propagation constants as

$$\gamma_n^{(1)} = \sqrt{(k_1)^2 - \left(\kappa_n^{(1)}\right)^2}. \tag{6}$$

Once we have obtained the relevant propagation constants, the secondary incident field $\mathbf{H}_1^+$ is calculated from Faraday's law, $\nabla \times \mathbf{E} = -j\omega\mu_0\mu_{r1}\mathbf{H}$. Letting $\mu_1 = \mu_0\mu_{r1}$, the result is readily found to be

$$\mathbf{H}_1^+(x,y) = \frac{1}{\omega\mu_1} \sum_{n=1}^{\infty} a_n \left[\hat{\mathbf{x}}\, j\kappa_n^{(1)} \phi_n^{(1)} - \hat{\mathbf{y}}\, \gamma_n^{(1)} \psi_n^{(1)}\right] e^{-j\gamma_n^{(1)} x}, \tag{7}$$

where the nth basis function $\phi_n^{(1)}$ is given as

$$\phi_n^{(1)} = \begin{cases} \cos\left(\kappa_n^{(1)}(y - y_1)\right) & y \in [y_1, H_1] \\ 0 & \text{otherwise} \end{cases} \tag{8}$$

The next step is to repeat the above analysis for the reverse-propagating wave. In this case, the primary field is given by

TABLE 1. A complete summary of all forward- and reverse-propagating field profiles under both TE and TM polarization. TM summations are taken from $n = 1$ to $n = N$. TE summations are taken from $n = 0$ to $n = N$.

Field Profile	Primary Series	Secondary Series
$\mathbf{E}_1^+(x,y)$	$\hat{\mathbf{z}}\sum a_n\psi_n^{(1)}e^{-j\gamma_n^{(1)}x}$	$\frac{1}{\omega\epsilon_{c1}}\sum a_n\left[\hat{\mathbf{x}}\,j\kappa_n^{(1)}\psi_n^{(1)}+\hat{\mathbf{y}}\,\gamma_n^{(1)}\phi_n^{(1)}\right]e^{-j\gamma_n^{(1)}x}$
$\mathbf{E}_1^-(x,y)$	$\hat{\mathbf{z}}\sum b_n\psi_n^{(1)}e^{+j\gamma_n^{(1)}x}$	$\frac{1}{\omega\epsilon_{c1}}\sum b_n\left[\hat{\mathbf{x}}\,j\kappa_n^{(1)}\psi_n^{(1)}-\hat{\mathbf{y}}\,\gamma_n^{(1)}\phi_n^{(1)}\right]e^{+j\gamma_n^{(1)}x}$
$\mathbf{E}_2^+(x,y)$	$\hat{\mathbf{z}}\sum c_n\psi_n^{(1)}e^{-j\gamma_n^{(2)}x}$	$\frac{1}{\omega\epsilon_{c2}}\sum c_n\left[\hat{\mathbf{x}}\,j\kappa_n^{(2)}\psi_n^{(2)}+\hat{\mathbf{y}}\,\gamma_n^{(2)}\phi_n^{(2)}\right]e^{-j\gamma_n^{(2)}x}$
$\mathbf{E}_2^-(x,y)$	$\hat{\mathbf{z}}\sum d_n\psi_n^{(1)}e^{+j\gamma_n^{(2)}x}$	$\frac{1}{\omega\epsilon_{c2}}\sum d_n\left[\hat{\mathbf{x}}\,j\kappa_n^{(2)}\psi_n^{(2)}-\hat{\mathbf{y}}\,\gamma_n^{(2)}\phi_n^{(2)}\right]e^{+j\gamma_n^{(2)}x}$
$\mathbf{H}_1^+(x,y)$	$\hat{\mathbf{z}}\sum a_n\phi_n^{(1)}e^{-j\gamma_n^{(1)}x}$	$\frac{1}{\omega\mu_1}\sum a_n\left[\hat{\mathbf{x}}\,j\kappa_n^{(1)}\phi_n^{(1)}-\hat{\mathbf{y}}\,\gamma_n^{(1)}\psi_n^{(1)}\right]e^{-j\gamma_n^{(1)}x}$
$\mathbf{H}_1^-(x,y)$	$\hat{\mathbf{z}}\sum b_n\phi_n^{(1)}e^{+j\gamma_n^{(1)}x}$	$\frac{1}{\omega\mu_1}\sum b_n\left[\hat{\mathbf{x}}\,j\kappa_n^{(1)}\phi_n^{(1)}+\hat{\mathbf{y}}\,\gamma_n^{(1)}\psi_n^{(1)}\right]e^{+j\gamma_n^{(1)}x}$
$\mathbf{H}_2^+(x,y)$	$\hat{\mathbf{z}}\sum c_n\phi_n^{(2)}e^{-j\gamma_n^{(2)}x}$	$\frac{1}{\omega\mu_2}\sum c_n\left[\hat{\mathbf{x}}\,j\kappa_n^{(2)}\phi_n^{(2)}-\hat{\mathbf{y}}\,\gamma_n^{(2)}\psi_n^{(2)}\right]e^{-j\gamma_n^{(2)}x}$
$\mathbf{H}_2^-(x,y)$	$\hat{\mathbf{z}}\sum d_n\phi_n^{(2)}e^{+j\gamma_n^{(2)}x}$	$\frac{1}{\omega\mu_2}\sum d_n\left[\hat{\mathbf{x}}\,j\kappa_n^{(2)}\phi_n^{(2)}+\hat{\mathbf{y}}\,\gamma_n^{(2)}\psi_n^{(2)}\right]e^{+j\gamma_n^{(2)}x}$

$\mathbf{E}_1^-$, and $\mathbf{H}_1^-$ serves as the corresponding secondary field. We then repeat the process for Region 2 by defining the primary fields as $\mathbf{E}_2^+$ and $\mathbf{E}_2^-$ with secondary fields $\mathbf{H}_2^+$ and $\mathbf{H}_2^-$. Finally, the whole process must repeat once again for TE polarization with primary fields $\mathbf{H}_1^+$, $\mathbf{H}_1^-$, $\mathbf{H}_2^+$, and $\mathbf{H}_2^-$. The result of that analysis is summarized in Table 1, which lists all primary and secondary field expressions under both polarizations.

3. BOUNDARY CONDITIONS

The ideal solution for **b** and **c** is one that satisfies the following conditions along $x = 0$:

1. Tangential E-field is zero along waveguide walls:

$$\mathbf{E}\cdot\hat{\mathbf{y}} = 0\Big|_{y\in\text{PEC}}, \quad \mathbf{E}\cdot\hat{\mathbf{z}} = 0\Big|_{y\in\text{PEC}} \tag{9}$$

2. Normal H-field is zero along waveguide walls:

$$\mathbf{H}\cdot\hat{\mathbf{x}} = 0\Big|_{y\in\text{PEC}} \tag{10}$$

3. Tangential E-field is continuous across the aperture:

$$\mathbf{E}_1\cdot\hat{\mathbf{y}} = \mathbf{E}_2\cdot\hat{\mathbf{y}}\Big|_{y\in\text{Aperture}}, \quad \mathbf{E}_1\cdot\hat{\mathbf{z}} = \mathbf{E}_2\cdot\hat{\mathbf{z}}\Big|_{y\in\text{Aperture}} \tag{11}$$

4. Tangential H-field is continuous across the aperture:

$$\mathbf{H}_1\cdot\hat{\mathbf{y}} = \mathbf{H}_2\cdot\hat{\mathbf{y}}\Big|_{y\in\text{Aperture}}, \quad \mathbf{H}_1\cdot\hat{\mathbf{z}} = \mathbf{H}_2\cdot\hat{\mathbf{z}}\Big|_{y\in\text{Aperture}} \tag{12}$$

5. Normal E-field across the aperture satisfies:

$$\epsilon_{c1}\mathbf{E}_1\cdot\hat{\mathbf{x}} = \epsilon_{c2}\mathbf{E}_2\cdot\hat{\mathbf{x}}\Big|_{y\in\text{Aperture}} \tag{13}$$

6. Normal H-field across the aperture satisfies:

$$\mu_1\mathbf{H}_1\cdot\hat{\mathbf{x}} = \mu_2\mathbf{H}_2\cdot\hat{\mathbf{x}}\Big|_{y\in\text{Aperture}} \tag{14}$$

An important property of electromagnetic waves is that any mathematical function which satisfies the above conditions is necessarily unique. That is to say, there is only one possible solution to our problem, and we can be sure that it is "correct" by the degree to which the boundary conditions are met. We therefore seek to quantify this error mathematically and then minimize it for a given set of mode vectors.

4. MEAN SQUARED ERROR: TM POLARIZATION

Consider a TM-polarized wave as it excites the waveguide junction depicted in Figure 1. According to our first boundary condition, the total tangential E-field must be zero along the waveguide walls. In Region 1 ($x = 0^+$), this implies $\mathbf{E}_1^+ + \mathbf{E}_1^- = 0$ along the metallic portion of the junction at $x = 0$. Since N is finite, however, it is not generally possible to satisfy such a condition over all y-values. Instead, the quantity $(\mathbf{E}_1^+ + \mathbf{E}_1^-)$ may be nonzero across the metal wall, which is an undesirable error in our solution. This motivates us to define the error function $\text{err}_{z,1}$ such that

$$\begin{aligned}\text{err}_{z,1}(y) &= \hat{\mathbf{z}}\cdot\mathbf{E}_1^+(0,y) + \hat{\mathbf{z}}\cdot\mathbf{E}_1^-(0,y)\\ &= \sum_{n=1}^{N}(a_n+b_n)\psi_n^{(1)} \qquad (y\in\text{PEC}).\end{aligned} \tag{15}$$

In Region 2, a similar argument applies to any nonzero value of $\mathbf{E}_2^+ + \mathbf{E}_2^-$ that likewise falls upon the perfect electrical conductor (PEC) walls at $x = 0$. We therefore define another error function $\text{err}_{z,2}(y)$ such that

$$\text{err}_{z,2}(y) = \sum_{n=1}^{N}(c_n+d_n)\psi_n^{(2)} \qquad (y\in\text{PEC}). \tag{16}$$

Finally, we need to quantify the error across the aperture. In this case, "error" is defined as any mismatch between the two fields at $x = 0$. We therefore define a third error function to capture this condition, which is written as

$$\text{err}_{z,3}(y) = \sum_{n=1}^{N}(a_n + b_n)\psi_n^{(1)} - \sum_{n=1}^{N}(c_n + d_n)\psi_n^{(2)} \qquad (y \in \text{Aperture}). \tag{17}$$

Now that we have formally defined the error across all relevant boundaries, the next step is to calculate the squared magnitude. This has the effect of treating both negative and positive errors as the same. For the first error function, this is written as

$$|\text{err}_{z,1}|^2 = (\text{err}_{z,1})^*(\text{err}_{z,1}), \tag{18}$$

where the asterisk $(*)$ indicates the complex conjugate. Applying similar expressions to $\text{err}_{z,2}$ and $\text{err}_{z,3}$, we add all terms together to arrive at the total squared error for the tangential electric field:

$$|\text{err}_z(y)|^2 = |\text{err}_{z,1}|^2 + |\text{err}_{z,2}|^2 + |\text{err}_{z,3}|^2. \tag{19}$$

We are now ready to define a metric on the squared-error function by mapping it to a single real-valued number. Although many such metrics are possible in theory, the Fourier series is uniquely well-suited for the classic **mean squared error** (MSE). We therefore define the MSE on the tangential electric field (E_z) as

$$\text{MSE}_z = \int_{y_L}^{y_H} |\text{err}_z(y)|^2 dy, \tag{20}$$

where y_L and y_H indicate the lower and upper limits of the entire waveguide junction. For the constricted waveguide depicted in Figure 1, these would be given as $y_L = y_1$ and $y_H = H_1$. More generally, however, the limits should satisfy

$$y_L = \min(y_1, y_2), \qquad \text{and} \tag{21}$$
$$y_H = \max(H_1, H_2). \tag{22}$$

The next step is to formally calculate MSE_z by substituting Eqs. (15)–(17) into Eq. (20). To help simplify matters, it will be useful to first define a special **unit aperture function** $u(y)$ such that

$$u(y) = \begin{cases} 1 & y \in \text{Aperture}\,, \\ 0 & \text{otherwise}\,. \end{cases} \tag{23}$$

It is further useful to define the **unit PEC function** as $\hat{u} = 1 - u$, which is only nonzero for y-values that land on the PEC walls. This allows us to implicitly calculate all integrals across the interval $[y_L, y_H]$, and the total mean squared error becomes

$$\begin{aligned}\text{MSE}_z = {} & + \int \hat{u}(y) \left[\sum_{n=1}^{N}(a_n^* + b_n^*)\psi_n^{(1)}\right] \left[\sum_{n=1}^{N}(a_n + b_n)\psi_n^{(1)}\right] dy \\ & + \int u(y) \left[\sum_{n=1}^{N}(a_n^* + b_n^*)\psi_n^{(1)} - (c_n^* + d_n^*)\psi_n^{(2)}\right] \left[\sum_{n=1}^{N}(a_n + b_n)\psi_n^{(1)} - (c_n + d_n)\psi_n^{(2)}\right] dy \\ & + \int \hat{u}(y) \left[\sum_{n=1}^{N}(c_n^* + c_n^*)\psi_n^{(2)}\right] \left[\sum_{n=1}^{N}(c_n + d_n)\psi_n^{(2)}\right] dy. \end{aligned} \tag{24}$$

While somewhat imposing at first glance, the above expression is actually quite tractable. Using standard matrix-vector notation, the entire expression is simplified neatly as

$$\begin{aligned}\text{MSE}_z = {} & +(\boldsymbol{a} + \mathbf{b})^H \mathbf{Z}_{11}(\boldsymbol{a} + \mathbf{b}) - (\boldsymbol{a} + \mathbf{b})^H \mathbf{Z}_{12}(\mathbf{c} + \mathbf{d}) \\ & -(\mathbf{c} + \mathbf{d})^H \mathbf{Z}_{21}(\boldsymbol{a} + \mathbf{b}) + (\mathbf{c} + \mathbf{d})^H \mathbf{Z}_{22}(\mathbf{c} + \mathbf{d}), \end{aligned} \tag{25}$$

where $\mathbf{x}^H$ indicates the conjugate transpose. The four **coupling matrices** are then given as

$$\mathbf{Z}_{11}\Big|_{nm} = \int_{y_1}^{H_1} \psi_n^{(1)}\psi_m^{(1)} dy,$$

$$\mathbf{Z}_{12}\Big|_{nm} = \int_{y_L}^{y_H} u(y)\psi_n^{(1)}\psi_m^{(2)} dy,$$

$$\mathbf{Z}_{21}\Big|_{nm} = \int_{y_L}^{y_H} u(y)\psi_n^{(2)}\psi_m^{(1)} dy,$$

$$\mathbf{Z}_{22}\Big|_{nm} = \int_{y_2}^{H_2} \psi_n^{(2)}\psi_m^{(2)} dy.$$

where $|_{nm}$ indicates the nth row and the mth column of the specified matrix.

Looking closely, we see that $\mathbf{Z}_{11}$ is calculated strictly over the interval from $[y_1, H_1]$. By the orthogonality of basis functions, however, this means that every element is zero except for $n = m$. Thus, $\mathbf{Z}_{11}$ is actually a diagonal matrix where each nonzero element is $h_1/2$. By the same argument, we may further deduce that $\mathbf{Z}_{22}$ is likewise a diagonal matrix with elements $h_2/2$. Finally, due to the symmetry of indexes, it is apparent that $\mathbf{Z}_{21} = \mathbf{Z}_{12}^T$.

Now that we are finished quantifying the MSE for the $\mathbf{E}_z$ boundary condition, we turn our attention to the H_y condition. Since we are only concerned about continuity across the aperture, we can ignore the PEC walls entirely and define the error function $\text{err}_y(y)$ as

$$\text{err}_y(y) = u(y)\frac{1}{\omega\mu_1}\sum_{n=1}^{N}(a_n - b_n)\gamma_n^{(1)}\psi_n^{(1)}$$

$$-u(y)\,\frac{1}{\omega\mu_2}\sum_{n=1}^{N}(c_n-d_n)\gamma_n^{(2)}\psi_n^{(2)}. \quad (26)$$

Following a similar derivation to the one used with MSE_z, we define a corresponding mean-squared error MSE_y along the y-component of the field profile, which is evaluated as

$$\begin{aligned}\mathrm{MSE}_y \;=\; &+(\boldsymbol{a}-\mathbf{b})^H\mathbf{K}_1^H\mathbf{Y}_{11}\mathbf{K}_1(\boldsymbol{a}-\mathbf{b})\\ &-(\boldsymbol{a}-\mathbf{b})^H\mathbf{K}_1^H\mathbf{Y}_{12}\mathbf{K}_2(\mathbf{c}-\mathbf{d})\\ &-(\mathbf{c}-\mathbf{d})^H\mathbf{K}_2^H\mathbf{Y}_{21}\mathbf{K}_1(\boldsymbol{a}-\mathbf{b})\\ &+(\mathbf{c}-\mathbf{d})^H\mathbf{K}_2^H\mathbf{Y}_{22}\mathbf{K}_2(\mathbf{c}-\mathbf{d}). \quad (27)\end{aligned}$$

In this case, the coupling matrices are all found to satisfy

$$\mathbf{Y}_{\ell k}\Big|_{nm}=\int_{y_L}^{y_H}u(y)\psi_n^{(\ell)}\psi_m^{(k)}dy. \quad (28)$$

The propagation matrices $\mathbf{K}_1$ and $\mathbf{K}_2$ are then written as diagonal matrices with elements given by

$$\mathbf{K}_\ell\Big|_{nn}=\frac{\gamma_n^{(\ell)}}{\omega\mu_\ell}. \quad (29)$$

Finally, we repeat the entire argument a third time to arrive at the mean squared error for the H_x boundary condition. Skipping to the end results in

$$\begin{aligned}\mathrm{MSE}_x \;=\; &+(\boldsymbol{a}+\mathbf{b})^H\mathbf{Q}_1^H\mathbf{X}_{11}\mathbf{Q}_1(\boldsymbol{a}+\mathbf{b})\\ &-(\boldsymbol{a}+\mathbf{b})^H\mathbf{Q}_1^H\mathbf{X}_{12}\mathbf{Q}_2(\mathbf{c}+\mathbf{d})\\ &-(\mathbf{c}+\mathbf{d})^H\mathbf{Q}_2^H\mathbf{X}_{21}\mathbf{Q}_1(\boldsymbol{a}+\mathbf{b})\\ &+(\mathbf{c}+\mathbf{d})^H\mathbf{Q}_2^H\mathbf{X}_{22}\mathbf{Q}_2(\mathbf{c}+\mathbf{d}). \quad (30)\end{aligned}$$

The $\mathbf{X}$ coupling matrices follow a similar format to $\mathbf{Z}$, but with the cosine basis functions instead of sines. Writing them out yields

$$\begin{aligned}\mathbf{X}_{11}\Big|_{nm} &= \int_{y_1}^{H_1}\phi_n^{(1)}\phi_m^{(1)}dy,\\ \mathbf{X}_{12}\Big|_{nm} &= \int_{y_L}^{y_H}u(y)\phi_n^{(1)}\phi_m^{(2)}dy,\\ \mathbf{X}_{21}\Big|_{nm} &= \int_{y_L}^{y_H}u(y)\phi_n^{(2)}\phi_m^{(1)}dy,\\ \mathbf{X}_{22}\Big|_{nm} &= \int_{y_2}^{H_2}\phi_n^{(2)}\phi_m^{(2)}dy.\end{aligned}$$

Following a similar argument as before, we deduce that $\mathbf{X}_{11}$ and $\mathbf{X}_{22}$ are diagonal matrices with elements given by $h_1/2$ and $h_2/2$, respectively. Likewise, $\mathbf{X}_{12}=\mathbf{X}_{21}^T$. The propagation matrices $\mathbf{Q}_1$ and $\mathbf{Q}_2$ are then given as

$$\mathbf{Q}_\ell\Big|_{nn}=\frac{\kappa_n^{(\ell)}}{\omega\mu_0}. \quad (31)$$

5. MINIMUM MEAN SQUARED ERROR: TM POLARIZATION

Now that we have formally defined the MSEs along each boundary condition, we are ready to combine them all into a single bulk error for the entire waveguide boundary. This is accomplished by weighing each individual error and then adding them all together:

$$\mathrm{MSE}=w_x\mathrm{MSE}_x+w_y\mathrm{MSE}_y+w_z\mathrm{MSE}_z. \quad (32)$$

In theory, the error weights (w_x,w_y,w_z) are arbitrary, and they may be customized to prefer one field component over the others. In practice, however, the ideal values should be chosen to best match the physically correct outcome. This problem will be explored further in Section 7.

Now that MSE has been quantified across the junction, the final step is to simply take the appropriate derivatives and then set them to zero. However, due to the complex values of our mode vectors, we need to be careful with how we exercise the rules of matrix-vector calculus. For our purposes, it is sufficient to think of the complex-valued vector derivative as two separate derivatives given by

$$\frac{\partial}{\partial\mathbf{b}}=\frac{\partial}{\partial\mathbf{b}_r}+j\frac{\partial}{\partial\mathbf{b}_i}, \quad (33)$$

where $\mathbf{b}_r$ and $\mathbf{b}_i$ indicate the real and imaginary components of $\mathbf{b}$. In general, this interpretation is not universal, but it functions for our specific application. Furthermore, the property $\mathbf{Z}_{11}=\mathbf{Z}_{11}^H$ is very important, as it means that the following identity applies:

$$\frac{\partial}{\partial\mathbf{b}}(\boldsymbol{a}+\mathbf{b})^H\mathbf{Z}_{11}(\boldsymbol{a}+\mathbf{b})=2\mathbf{Z}_{11}(\boldsymbol{a}+\mathbf{b}). \quad (34)$$

Likewise, because $\mathbf{Z}_{12}=\mathbf{Z}_{21}^H$, we can write another useful identity:

$$\begin{aligned}&\frac{\partial}{\partial\mathbf{b}}\left[(\boldsymbol{a}+\mathbf{b})^H\mathbf{Z}_{12}(\mathbf{c}+\mathbf{d})+(\mathbf{c}+\mathbf{d})^H\mathbf{Z}_{21}(\boldsymbol{a}+\mathbf{b})\right]\\ &=\;2\mathbf{Z}_{21}(\mathbf{c}+\mathbf{d}). \quad (35)\end{aligned}$$

We now have enough information to summarize the following results:

$$\frac{\partial}{\partial\mathbf{b}}\mathrm{MSE}_x=+2\mathbf{Q}_1^H\mathbf{X}_{11}\mathbf{Q}_1(\boldsymbol{a}+\mathbf{b})-2\mathbf{Q}_1^H\mathbf{X}_{12}\mathbf{Q}_2(\mathbf{c}+\mathbf{d}) \quad (36)$$

$$\frac{\partial}{\partial\mathbf{b}}\mathrm{MSE}_y=-2\mathbf{K}_1^H\mathbf{Y}_{11}\mathbf{K}_1(\boldsymbol{a}-\mathbf{b})+2\mathbf{K}_1^H\mathbf{Y}_{12}\mathbf{K}_2(\mathbf{c}-\mathbf{d}) \quad (37)$$

$$\frac{\partial}{\partial\mathbf{b}}\mathrm{MSE}_z=+2\mathbf{Z}_{11}(\boldsymbol{a}+\mathbf{b})-2\mathbf{Z}_{12}(\mathbf{c}+\mathbf{d}) \quad (38)$$

Repeat by calculating the vector derivative of each error term with respect to $\mathbf{c}$:

$$\frac{\partial}{\partial\mathbf{c}}\mathrm{MSE}_x=+2\mathbf{Q}_2^H\mathbf{X}_{22}\mathbf{Q}_2(\mathbf{c}+\mathbf{d})-2\mathbf{Q}_2^H\mathbf{X}_{21}\mathbf{Q}_1(\boldsymbol{a}+\mathbf{b}) \quad (39)$$

$$\frac{\partial}{\partial\mathbf{c}}\mathrm{MSE}_y=-2\mathbf{K}_2^H\mathbf{Y}_{22}\mathbf{K}_2(\mathbf{c}-\mathbf{d})+2\mathbf{K}_2^H\mathbf{Y}_{21}\mathbf{K}_1(\boldsymbol{a}-\mathbf{b}) \quad (40)$$

$$\frac{\partial}{\partial \mathbf{c}}\mathrm{MSE}_z = +2\mathbf{Z}_{22}(\mathbf{c}+\mathbf{d}) - 2\mathbf{Z}_{21}(\boldsymbol{a}+\mathbf{b}) \tag{41}$$

The final step is to combine these derivatives together and then set their sums to zero. The results are compiled into a single block matrix-vector equation with the form of

$$\begin{bmatrix}\mathbf{G}_{11} & \mathbf{G}_{12}\\ \mathbf{G}_{21} & \mathbf{G}_{22}\end{bmatrix}\begin{bmatrix}\mathbf{b}\\ \mathbf{c}\end{bmatrix} = \begin{bmatrix}\mathbf{A}_b\boldsymbol{a}\\ \mathbf{A}_c\boldsymbol{a}\end{bmatrix} + \begin{bmatrix}\mathbf{D}_b\mathbf{d}\\ \mathbf{D}_c\mathbf{d}\end{bmatrix}, \tag{42}$$

where each sub-matrix element is given as

$$\mathbf{G}_{11} = +w_x\mathbf{Q}_1^H\mathbf{X}_{11}\mathbf{Q}_1 + w_y\mathbf{K}_1^H\mathbf{Y}_{11}\mathbf{K}_1 + w_z\mathbf{Z}_{11} \tag{43}$$
$$\mathbf{G}_{12} = -w_x\mathbf{Q}_1^H\mathbf{X}_{12}\mathbf{Q}_2 + w_y\mathbf{K}_1^H\mathbf{Y}_{12}\mathbf{K}_2 - w_z\mathbf{Z}_{12} \tag{44}$$
$$\mathbf{G}_{21} = -w_x\mathbf{Q}_2^H\mathbf{X}_{21}\mathbf{Q}_1 + w_y\mathbf{K}_2^H\mathbf{Y}_{21}\mathbf{K}_1 - w_z\mathbf{Z}_{21} \tag{45}$$
$$\mathbf{G}_{22} = +w_x\mathbf{Q}_2^H\mathbf{X}_{22}\mathbf{Q}_2 + w_y\mathbf{K}_2^H\mathbf{Y}_{22}\mathbf{K}_2 + w_z\mathbf{Z}_{22} \tag{46}$$
$$\mathbf{A}_b = -w_x\mathbf{Q}_1^H\mathbf{X}_{11}\mathbf{Q}_1 + w_y\mathbf{K}_1^H\mathbf{Y}_{11}\mathbf{K}_1 - w_z\mathbf{Z}_{11} \tag{47}$$
$$\mathbf{A}_c = +w_x\mathbf{Q}_2^H\mathbf{X}_{21}\mathbf{Q}_1 + w_y\mathbf{K}_2^H\mathbf{Y}_{21}\mathbf{K}_1 + w_z\mathbf{Z}_{21} \tag{48}$$
$$\mathbf{D}_b = +w_x\mathbf{Q}_1^H\mathbf{X}_{12}\mathbf{Q}_2 + w_y\mathbf{K}_1^H\mathbf{Y}_{12}\mathbf{K}_2 + w_z\mathbf{Z}_{11} \tag{49}$$
$$\mathbf{D}_c = -w_x\mathbf{Q}_2^H\mathbf{X}_{22}\mathbf{Q}_2 + w_y\mathbf{K}_2^H\mathbf{Y}_{22}\mathbf{K}_2 - w_z\mathbf{Z}_{22} \tag{50}$$

We now solve for **b** and **c** to arrive at the solution for **minimum mean squared error** (MMSE):

$$\boxed{\begin{bmatrix}\mathbf{b}\\ \mathbf{c}\end{bmatrix} = \begin{bmatrix}\mathbf{G}_{11} & \mathbf{G}_{12}\\ \mathbf{G}_{21} & \mathbf{G}_{22}\end{bmatrix}^{-1}\left(\begin{bmatrix}\mathbf{A}_b\boldsymbol{a}\\ \mathbf{A}_c\boldsymbol{a}\end{bmatrix} + \begin{bmatrix}\mathbf{D}_b\mathbf{d}\\ \mathbf{D}_c\mathbf{d}\end{bmatrix}\right)}. \tag{51}$$

6. MEAN SQUARED ERROR: TE POLARIZATION

The procedure for TE polarization follows an identical argument for TM. Begin by writing out the error function for H_z, which only requires continuity across the aperture:

$$\mathrm{err}_z(y) = u(y)\sum_{n=0}^{N}(a_n+b_n)\phi_n^{(1)} - u(y)\sum_{n=0}^{N}(c_n+d_n)\phi_n^{(2)}. \tag{52}$$

For the y-component of the E-field, we require continuity across the aperture, plus zero tangential fields along the PEC walls:

$$\mathrm{err}_{y,1}(y) = \frac{\hat{u}(y)}{\omega\epsilon_{c1}}\sum_{n=0}^{N}(a_n-b_n)\gamma_n^{(1)}\phi_n^{(1)} \tag{53}$$

$$\mathrm{err}_{y,2}(y) = \frac{\hat{u}(y)}{\omega\epsilon_{c2}}\sum_{n=0}^{N}(c_n-d_n)\gamma_n^{(2)}\phi_n^{(2)} \tag{54}$$

$$\mathrm{err}_{y,3}(y) = \frac{u(y)}{\omega\epsilon_{c1}}\sum_{n=0}^{N}(a_n-b_n)\gamma_n^{(1)}\phi_n^{(1)} - \frac{u(y)}{\omega\epsilon_{c2}}\sum_{n=0}^{N}(c_n-d_n)\gamma_n^{(2)}\phi_n^{(2)}. \tag{55}$$

Finally, the x-component of the E-field follows Eq. (13), leading to

$$\mathrm{err}_x(y) = \frac{u(y)}{\omega\epsilon_0}\sum_{n=0}^{N}(a_n+b_n)\kappa_n^{(1)}\psi_n^{(1)} - \frac{u(y)}{\omega\epsilon_0}\sum_{n=0}^{N}(c_n+d_n)\kappa_n^{(2)}\psi_n^{(2)}. \tag{56}$$

Notice how this is identical in form to the TM case, but with a few modified terms. The equations for MSE and MMSE therefore take on the exactly same structure as before. The only differences are (1) the basis functions in each coupling matrix element, (2) the limits of integration, and (3) the diagonal propagation matrices.

7. DEMONSTRATION

This section showcases an example calculation of the field profile for a stepped waveguide discontinuity. The waveguide heights were set to $h_1 = h_2 = 15\,\mathrm{cm}$ with floor offsets of $y_1 = 0$ and $y_2 = -6\,\mathrm{cm}$. The waveguide was excited from the left at a frequency of $f_0 = 1.5\,\mathrm{GHz}$ with a fundamental mode amplitude of $a_1 = 1.0\,\mathrm{V/m}$ (all other amplitudes were zero). For simplicity, the waveguide interior was filled with free space, and a total of $N = 100$ modes were used in the calculation.

Figure 2 depicts the complete electric field profile. Notice the particular choice of an offset waveguide, which is not a scenario that can be accurately modeled by a direct application of mode orthogonality. For comparison, a numerical simulation was also performed using the FDTD method under identical conditions. For consistency, both field profiles were normalized to unit amplitude. Also, since FDTD is inherently a time-domain method, the MMM profile required manual phase adjustment to align with the simulation results (≈ 0.275 radians).

Running MATLAB on a standard desktop computer, the mode-matching program required about 90 ms to generate all system matrices, invert them, and then unpack the resulting mode vectors for **b** and **c**. In contrast, the FDTD simulation required 86 sec to complete on a similar (unparallelized) desktop

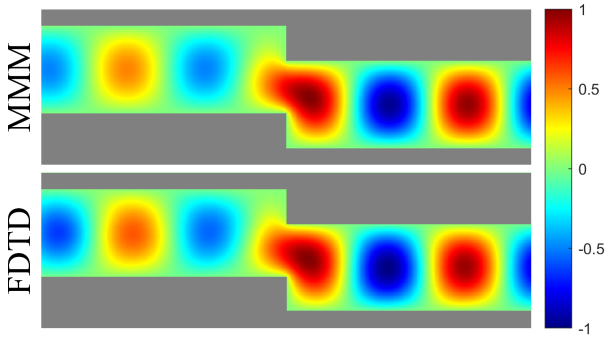

FIGURE 2. Normalized electric field profile for a TM-polarized wave as it excites a parallel plate waveguide boundary from the left. The top profile depicts the mode-matching method (MMM) while the bottom shows the equivalent results from FDTD simulation.

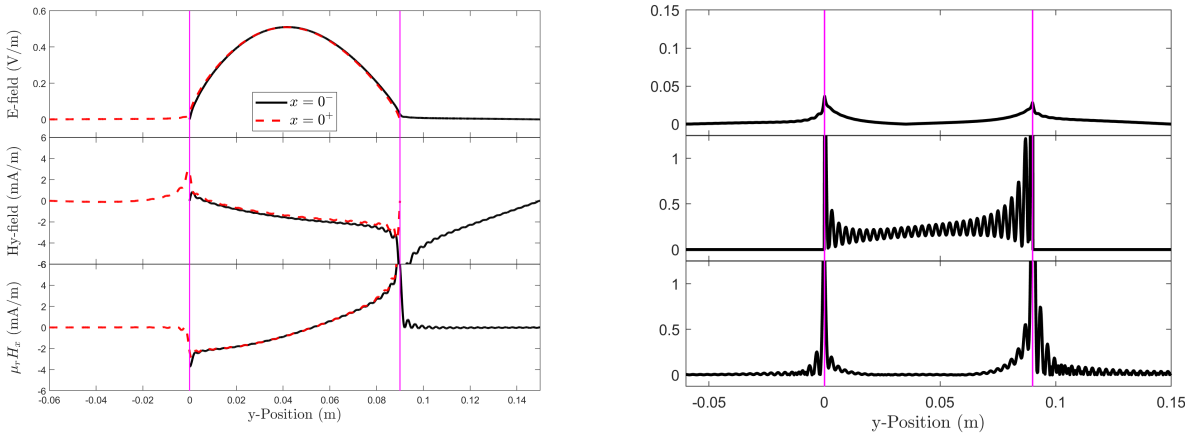

FIGURE 3. Field continuity profiles along the $x = 0$ boundary. The left figure shows the instantaneous profiles for both the electric and magnetic fields. Black lines indicate the field profile immediately to the left of the boundary in Region 1 ($x = 0^-$) while the red lines indicate the fields immediately to right in Region 2 ($x = 0^+$). The right figure plots the absolute value of the corresponding error function for each field profile.

computer. Results appear to confirm the accuracy of MMM, with most observable error being attributable to FDTD discretization and some minor phase mismatch.

The choice of weight coefficients is not straightforward, but the search space can be narrowed down through careful consideration. Most notably, the H-field magnitude of a uniform plane wave in a lossless medium satisfies $|H| = |E|/\eta_0$, where $\eta = \sqrt{\mu_0/\epsilon_0}$ is the intrinsic impedance of free space. For TM polarization, this motivates us to weigh the H-field errors by $w_x = w_y = \eta^2$ so as to normalize the relative scale of the squared fields (or the opposite weighting for TE polarization). In effect, we are attempting to treat one unit of error as the same for all field components, whether they are electric or magnetic. This choice immediately produces strong correlation with the FDTD simulation, but some noticeable discontinuities were still visible. After some trial-and-error, we finally settled on a value of $w_z = 10$ for this demonstration.

To further validate the solution, Figure 3 shows all components of the instantaneous field profiles along the boundary at $x = 0$. Per the uniqueness theorem, any solution that satisfies all specified boundary conditions simultaneously is also the mathematically desired outcome. Any failures in the mode-matching algorithm will therefore appear as a visual mismatch in the field profiles between $x = 0^+$ and $x = 0^-$. For convenience, we also include a plot of the absolute value of each corresponding error function, with the y-scale zoomed in for clarity.

As is typical of a Fourier series, the accuracy is best when the function is smooth and continuous. It is therefore expected for the mode-matching approximation to struggle at the boundaries of the aperture. Since the electric field is non-smooth at these points, we see that error naturally accumulates. In contrast, the H-field components are discontinuous, so error is extra pronounced at these points. We also see that the H-field exhibits the familiar Gibbs phenomenon as a result.

Another valuable feature of our new mode-matching technique is numerical stability. To demonstrate, the waveguide junction was solved over an ever-increasing value for the total

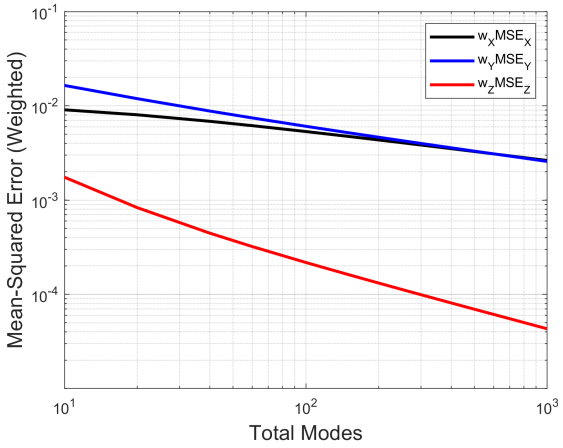

FIGURE 4. Weighted mean-squared error for each field profile as a function of total mode number N.

mode number N. Figure 4 shows the result of that calculation by plotting the weighted mean-squared error for each field profile as a function of N. As expected, the total mean-squared error steadily decreases as the total mode number N increases. We also see that the algorithm appears significantly more proficient at minimizing the E-field error. This is likely due to our preferential weighting of $w_z = 10$, as well as the discontinuity of the H-field profile being more difficult to match. In either case, the solution is also remarkably stable, as is evidenced by the condition number of the system matrix in Eq. (42). Even with the substantially large value of $N = 1000$ modes, the condition number was only 1.2×10^6, which is a relatively small value for such a large matrix.

8. DIELECTRIC-LOADED WAVEGUIDE

The dielectric-loaded waveguide is a common construction used to characterize the dielectric properties of engineered materials [10, 11]. In this section, we consider a waveguide junction that is filled with a lossy dielectric ($e_r = 9$, $\sigma = 0.05$). This situation is representative of a high dielec-

tric constant polymer nanocomposite with applications to RF-absorbing coatings [12]. Accurate modeling of this case is useful for calibrating measurement fixtures, and it can be solved using plane-wave reflection and transmission coefficients. This makes it a valuable benchmark for validating the numerical implementation in this paper.

Figure 5 depicts the normalized electric field profile for just such a loaded waveguide. The plate separation was set to $h_1 = h_2 = 10\,\text{cm}$ with an excitation frequency of 2.4 GHz. As with the previous example, only the fundamental mode excites the system from the left. Since the two waveguide plates have the same height, the system sub-matrices $\mathbf{G}_{11}$, $\mathbf{G}_{12}$, $\mathbf{G}_{21}$, and $\mathbf{G}_{22}$ are all diagonals, and there is no cross-coupling between mode numbers. Thus, a perfect solution can be obtained using just $N = 1$, exhibiting zero MSE in the boundary between regions. The reflected mode amplitude was thus found to be $b_1 = -0.5798 + 0.0072j$, which exactly corresponds to a reflection coefficient of $(\gamma_1^{(1)} - \gamma_1^{(2)})/(\gamma_1^{(1)} + \gamma_1^{(2)})$. Similarly, $c_1 = 0.4202 + 0.0072j$, which corresponds exactly with a transmission coefficient of $2\gamma_1^{(1)}/(\gamma_1^{(1)} + \gamma_1^{(2)})$.

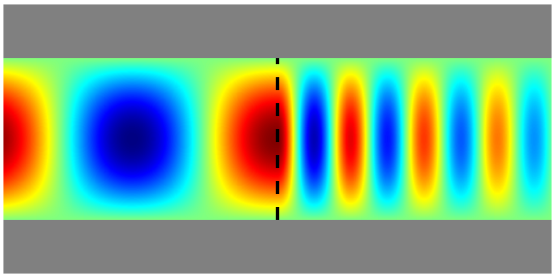

FIGURE 5. Normalized electric field profile for a TM-polarized wave as it excites a dielectric interface in a parallel-plate waveguide.

9. DISCUSSION

In this paper, we have introduced a new solution method based on the mode-matching method. The method works by minimizing the mean-squared error across electromagnetic boundary conditions at the waveguide discontinuity. The solution was demonstrated on the special case of an offset waveguide, which was then validated against numerical simulation. We also validated the method against a special case of the dielectric junction, which has an exact, closed-form solution. The technique generalizes well to a wide variety of possible junctions, including open/constricted waveguides, mismatched materials, and even single/multiple-slit irises. The only mathematical distinction between them is the aperture function of Eq. (23), which essentially determines the limits of integration in the mode-overlap integrals.

While a single waveguide junction has limited applications, a series cascade of many such junctions can be used in a wide variety of practical devices. The solution method presented in this paper is thus a building block. A useful follow-up study would expand upon the solution to construct a complete scattering matrix for the junction. Many such scattering matrices could be then combined into a single scattering matrix over the entire cascade. Calculation of the complete frequency response would then simply be a matter of repeating the calculation over a large number of excitation frequencies.

Once a complete scattering theory has been demonstrated, it should be possible to extend the analysis to the general case of a rectangular waveguide boundary in three dimensions. Mathematically, the procedure should be essentially the same, except for some added complexity of the additional dimension. From there, the basic procedure should likewise extend to more complex waveguide configurations like the right-angle bend, three-port junctions, dielectric slab, fiber-optic cables, or even mixed boundaries between entirely distinct waveguide types (e.g., rectangular waveguide coupled to a circular dielectric waveguide). Based on the preceding analysis, it seems likely that the greatest difficulty would arise from calculating basis functions, followed by their corresponding coupling integrals across the junction.

Moving forward, the most immediate gap in our understanding lies with the error weights. Although we demonstrated functional values in this publication, the choice was somewhat ad-hoc. It therefore remains a topic of future investigation to derive the mathematically optimal values over any arbitrary configuration of waveguide boundary.

REFERENCES

[1] Taflove, A. and S. C. Hagness, *Computational Electrodynamics: The Finite-Difference Time-Domain Method*, 3rd ed., Artech House, 2005.

[2] Jin, J.-M., *The Finite Element Method in Electromagnetics*, 3rd ed., Wiley-IEEE Press, 2014.

[3] Guglielmi, M., G. Conciauro, and R. Sorrentino, *Advanced Modal Analysis*, 1st ed., Wiley, 2000.

[4] Wexler, A., "Solution of waveguide discontinuities by modal analysis," *IEEE Transactions on Microwave Theory and Techniques*, Vol. 15, No. 9, 508–517, 1967.

[5] Read, W. W., "An analytic series method for laplacian problems with mixed boundary conditions," *Journal of Computational and Applied Mathematics*, Vol. 209, No. 1, 22–32, 2007.

[6] Nagel, J. R., "An analytic model for stripline/microstrip potential using infinite series with mixed boundary conditions," *Progress In Electromagnetics Research M*, Vol. 107, 231–242, 2022.

[7] Balanis, C. A., *Advanced Engineering Electromagnetics*, 2nd ed., Wiley, Hoboken, NJ, 2012.

[8] Jackson, J. D., *Classical Electrodynamics*, 3rd ed., Wiley, Hoboken, NJ, 1999.

[9] Pozar, D. M., *Microwave Engineering*, 4th ed., Wiley, 2012.

[10] Rothwell, E. J., J. L. Frasch, S. M. Ellison, P. Chahal, and R. O. Ouedraogo, "Analysis of the Nicolson-Ross-Weir method for characterizing the electromagnetic properties of engineered materials," *Progress In Electromagnetics Research*, Vol. 157, 31–47, 2016.

[11] Rohde & Schwarz, "Measurement of Dielectric Material Properties — RAC-0607-0019," Application Note, July 2012.

[12] Jiang, S., L. Jin, H. Hou, and L. Zhang, "Polymer-based nanocomposites with high dielectric permittivity," in *Polymer-Based Multifunctional Nanocomposites and Their Applications*, J. Z. G. Kenan Song, Chuntai Liu, ed., Ch. 8, 201-243, Elsevier, 2019.